scientific reports

Check for updates

OPEN

Parametric optimization of flow in a solar chimney power plant under variable semi elliptical constraints

Rajamurugu Natarajan[1], S. Yaknesh[2], K B Prakash[3], Mohammed Al Awadh[4,5] & Qasem M. Al-Mdallal[6]✉

In response to the ongoing quest for more efficient renewable energy sources, this research addresses a significant gap in understanding the performance variations of Solar Chimney Power Plant (SCPP) models, particularly focusing on the influence of flow parameters in full and half-inclined collector sections featuring semi-elliptical curvature. The motivation stems from the need to optimize SCPP designs for enhanced energy generation while minimizing resource utilization and environmental impact. This research focuses on investigating flow parameter variations in Solar Chimney Power Plant (SCPP) models with full and half-inclined collector sections featuring semi-elliptical curvature and variable semi-minor heights (b: 0.01–0.03 m). The six models, including divergent chimneys (4 m), collector diameter (2.6 m), and 0.04 m collector inlet height at a 10° positive inclination, were categorized into Full Inclined Semi Elliptical Solar Chimney Power Plants (FSCPP-1,2,3) and Half Inclined Semi Elliptical Solar Chimney Power Plant (HSCPP-1,2,3). Initially, ANSYS-FLUENT were utilized for computational approximation. The models with greater maximum flow parameter magnitudes were selected for experimentation. FSCPP-1 and HSCPP-1 demonstrated superior performance, achieving higher maximum velocities (4.31 m/s, 4.49 m/s) under a temperature rise of 35 K and 36 K. Experimental results aligned well with computational data. Validation with a straight tower inclined collector solar chimney (SSCPP) and existing literatures concluded that the semi-elliptical profile in the half-inclined collector model (HSCPP-1) enhances overall system performance. In addition, a comparison between computational and experimental approaches revealed an error approximation of up to 5%. FSCPP-1 outperformed its subgroup with velocity and temperature enhancements up to 5% and 2%, while HSCPP-1 surpassed its group with 4% and 1% enhancement. Validation with SSCPP highlighted the maximum velocity enhancements of up to 42% in FSCPP and 44% in HSCPP models. In higher flow parameter magnitude models, HSCPP-1 outperformed FSCPP-1 with a 4% enhancement in maximum velocity and up to 2% in temperature magnitude, emphasizing the positive influence of curvature heights (0.01–0.03 m) progressing towards minimal positive percentage enhancements.

Keywords Renewable Energy, Solar Chimney Power Plant, Divergent chimney, Inclined Collector, Semi-elliptic Profiles

Abbreviations

SCPP	Solar Chimney Power Plant
FSCPP	Full inclined Semi Elliptical Solar Chimney Power Plant
HSCPP	Half inclined Semi Elliptical Solar Chimney Power Plant
SSCPP	Straight tower inclined collector Solar Chimney Power Plant
SUT	Solar Updraft Tower
CFD	Computation Fluid Dynamics

[1]Department of Aeronautical and Aerospace Engineering, KCG College of Technology, Chennai, India. [2]Department of Aerospace Engineering, Chandigarh University, Gharuan, Punjab, India. [3]Department of Mechanical Engineering, Bannari Amman Institute of Technology, Sathyamangalam, Erode, Tamil Nadu, India. [4]Department of Industrial Engineering, College of Engineering, King Khalid University, P.O. Box 394, Abha 61421, Saudi Arabia. [5]Center for Engineering and Technology Innovations, King Khalid University, Abha 61421, Saudi Arabia. [6]Department of Mathematical Sciences, United Arab Emirates University, P.O. Box 15551, Al Ain, Abu Dhabi, United Arab Emirates. ✉email: q.almdallal@uaeu.ac.ae

Greek symbols

T	Temperature (K)
T_0	Ambient Temperature (K)
ρ	Density (kg/m^3)
ρ_0	Ambient Density (kg/m^3)
β	Expansion rate
A	Area (m^2)
u	Initial Velocity (m/s^2)
t	Time (s)
V	Velocity (m/s^2)
μ	Coefficient of viscosity
$\dot{m}$	Mass flow rate (kg/s)
$\triangle p$	Pressure difference (Pa)
ν	Final Velocity (m/s)
$\mathrm{e_t}$	Heat Transfer
$\overrightarrow{F_b}$	Body Force (N)
a	Absorptivity
b_λ	Intensity
s	Scattering Coefficient
n	Refractive Index
g	Acceleration due to gravity (m/s^2)
r	Radial Position in collector (m)
$\mathrm{r_d}$	Divergent sectional radius up to assumed chimney height
$\mathrm{r_i}$	Chimney inlet radius
x	Position along chimney from its inlet (m)
$\mathrm{R_{coll}}$	Collector Radius(m)
$\mathrm{r/R_{coll}}$	Collector radius ratio
$\mathrm{H_{chim}/r_d}$	Divergent sectional aspect ratio
$\mathrm{x/r_i}$	Positional ratio
$\mathrm{H_{chim}}$	Chimney Height(m)
$\mathrm{x/H_{chim}}$	Chimney Height ratio

Subscripts

d	Divergent section
i	Chimney inlet
max	Maximum
coll	Collector
chim	Chimney

The evolution of electricity demand from industrial to household applications has driven advancements in power production systems. Non-renewable sources dominate current energy generation, contributing to environmental issues[1]. The Solar Chimney Power Plant (SCPP) emerges as a promising alternative, harnessing buoyancy effects and natural convection for eco-friendly energy production. With a simple construction comprising a collector, chimney, ground, and turbine, the SCPP operates without fuel combustion. Solar radiation heats the ground beneath the transparent collector, initiating natural convection and creating an updraft through the chimney[2]. The updraft drives the turbine, which is connected to a generator for electricity production. Unlike complex conventional systems, SCPP requires no moving parts for flow initiation, making it an efficient and green technology[3].

The air static pressure at the chimney inlet, denoted as "Δp," is important for achieving optimal airflow rates in solar chimney power plants (SCPP)[4]. A study[5]estimated dynamic pressure distributions in SCPP, revealing a maximum potential pressure drop at 2/3rd of the chimney height under constant driving potential conditions[6]. Another parameter, such as chimney height and diameter, is identified as critical geometric parameters influencing airflow in solar chimneys[7]. A linear relationship was established with simulation results for two SCPP models (100 m and 500 m long) and found that efficiency varies linearly with an increase in chimney height[8]. A few studies highlighted that the collector radius was found to have a positive impact on power output and efficiency[9], but a negative impact on chimney height. Numerical simulations demonstrated that divergent chimney geometry enhances performance for improved power generation capability[10]. Studies[11]analyzed the influence of the aspect ratio on SCPP performance, concluding that a 4:1 aspect ratio leads to 168.5 kW of power with 0.83% efficiency. Another study[12] investigated the best configuration for a SCPP in terms of tower height and collector radius. The study has highlighted that the divergent chimney is an optimized one and yields better performance than the conventional one.

A mathematical stoichiometric model for the collector profile was developed in a study by incorporating assumptions for flow improvement[13]. Another study investigated the energy balance of solar collectors, considering frictional effects through a thermal network model[14]. The impact of thermal energy storage on SCPP performance was observed to be longer during the operational periods with a thermal storage system[15]. The effect of diffuser-type chimneys on the overall performance of the system has given insight into the modifications to chimney geometries[16]. Simulation studies on the SCPP showed an enhancement in average air velocity of 31% with an extended chimney height of 3 m to 8 m[17]. A computational analysis of different chimney configurations carried out in a study[18]found that the two-degree divergent chimney was the optimized one for

any divergent SCPP. For a cylindrical chimney, a study[19] validated two chimney bottom designs, noting a 38.5% increase in updraft velocity with a 45° fillet section.

On the modifications of collector design, a few studies[30]and[31]concluded that the half-convergent collector model (HCFD) outperforms other designs in maximum velocity, temperature rise, and power output. The table-1(a) and (b) summarises the key works carried out in recent times on investigating the effect of various geometric parameters on the performance of SCPP. Whereas table-1(c) presents the key works carried out using numerical techniques. Few experiment studies in the past have been carried out, including one on a pilot plant of a 5 m tall tower for 180 days, validated with numerical simulations[19]. Another study implemented measurements to estimate the overall performance of a small-scale prototype in Indonesia[53].

Experiment on a novel SCPP design with the parabolic profiles in the chimney as well as the collector found that there was an enhanced conventional chimney by 12%[32]. another study examined a boxed non-covered solar still with a thermoelectric condensing duct for improved water heating performance, suggesting the use of a dish concentrator for sustainable financial benefits[33]. An interesting work explored a hybrid Nano fluid for solar water heating with antibacterial properties[34]. The collector's geometry is pivotal in optimizing the buoyancy effect in Solar Chimney Power Plants (SCPP)[35]. It captures and refracts solar radiation, influencing the system's performance. Modifications to the collector geometry yielded some better performance than the conventional

(a)

Parameter	Observation	References
Chimney Height	Increasing height raises performance, but some researchers believe there's a limit to efficiency improvement.	20–23
Collector Radius	Increasing radius boosts power output, with exponential gains noted; however, a maximum performance point is suggested by some researchers.	24–27
Chimney Diameter	Larger diameters discharge more air but may reduce power output past an optimal size.	28,29
Collector Height	Greater height allows more air intake but negatively affects temperature increase under the collector.	30–32
Collector Slope	Increased slope (tilt) can enhance airflow and power output, but excessive slope may reduce performance.	33–36
Chimney Design	Divergent chimneys increase air discharge and performance; convergent designs decrease air discharge. Both designs impact system efficiency.	30,37,38

(b)

Aspect	Key Inferences	References
Chimney Height	Solar chimneys exceeding 1000 m are feasible; advancements make high-rise structures safer and more stable despite structural challenges.	13
Reinforcement	Chimneys up to 500 m can be constructed without ring reinforcement; higher chimneys need strong internal or wireless reinforcements.	13
Wall Thickness	Wall thickness decreases with height (e.g., 0.65 m at the base, 0.25 m at the top for a 1000 m chimney).	13
Chimney Diameter	Diameter reduces with height; for instance, a 1000 m chimney design tapers from 260 m at the base to 145 m at the top.	13
Material Selection	Varied materials, like PVC pipes, polycarbonate, and steel, are used for experimental chimneys, chosen for factors like impact resistance.	14–16
Experimental Designs	Smaller experimental chimneys include an 8 m PVC pipe with a 0.3 m diameter and a 15 m steel chimney with a cross-section of 1.92 m^2.	14,16
Wind Considerations	Assessing structural wind speeds and wind drag forces prior to installation is recommended for safety and stability.	17

(c)

Study	Model/Method Used	Key Values and Findings	References
Al-Kayiem and Al-Nakeeb	Finite Difference Technique	Convergent chimney design's hydrothermal efficiency is twice that of other designs.	18
Hu et al.	CFD Model	Ideal chimney exit area ratio (AR) to entrance area for maximum performance is about 10; exceeding this reduces efficiency.	19
Hassan et al.	Numerical Model (Manzanares Pilot Plant)	Power output increases with divergent chimney angle: 1° = 68 kW, 2° = 65 kW, 3° = 59 kW.	20
Ahirwar and Sharma	Based on Manzanares Pilot Plant Geometry	Optimal chimney height for maximum power output with inclined collector is 190 m; power output increases with 6° angle.	21
Pattanashetti and Madhukeshwara	1° Isometric CFD Model	For AR = 9, maximum performance achieved; chimney outlet diameters vary from 2.83 to 16 m.	22
Ghorbani et al.	Hybrid Design (Solar Chimney Format)	Diverging flue angle of 1.5° increases air velocity on radiators from 5.65 m/s to 6 m/s (6.2% increase).	23
Das and Candramohan	3D Computational Model (CFD)	Small-scale solar chimneys (7 m and 3.5 m); maximum power output and airflow achieved at a 2° divergent angle; larger angles reduce performance.	24
Xu and Zhou	CFD Study with TPP and EPPRC	Maximum power output at COAR = 8.7, yielding a 10.9x increase to 231.7 kW; COAR > 8.7 causes reverse flow, decreasing output and airflow velocity.	25
Koonsrisuk and Chitsomboon	5° Axial Symmetric CFD Model	For AR = 16, power output increases to 94.29 times the reference, with system efficiency reaching 25%; chimney height = 100 m, collector radius = 100 m.	26
Choi et al.	Analytical Model (validated by Manzanares Pilot Plant)	SCPP with water storage system reduces midday power output (from 35 kW to below 25 kW) but increases 24-hour total output; for large-scale system, max power output without storage > 80 MW, drops to < 60 MW with storage.	27
Yaswanthkumar and Chandramohan	3D CFD Model	Small-scale system (collector radius = 3.5 m, chimney height = 6 m) with TES shows lower air pressure, temperature, and velocity compared to design without TES.	28
Attig-Bahar et al.	3D CFD Model (based on Manzanares Pilot Plant)	Predicted performance of SCPP in Tozeur, Tunisia, with 5-m thick soil, gravel, and sand as heat storage materials; storage materials improve system performance.	29

Table 1. (**a**) Summary of key studies and their observations on collector. (**b**) Summary of key studies and their observations on chimney. (**c**) Summary of key CFD studies.

shapes. In an experimental study, it was found that increasing the tower height beyond 4 m did not produce any significant impact on the power output of a divergent chimney[36]. The technical feasibility of a solar tower, considering chimney height, humidity, and solar radiation[30]introduced the hanging metallic tubes inside the collector[37], investigated the flow pattern variation, and achieved an overall temperature rise of 5 K. Existing literatures extensively discusses the basic operational principles, computational studies, and experimental results of SCPPs. However, several aspects remain underexplored or could benefit from further refinement. Specifically, the geometry of the collector and chimney profiles has a profound impact on the performance and efficiency of SCPPs, yet optimal designs have not been fully realized. Additionally, while many studies have focused on traditional flat or slightly inclined collectors, the potential benefits of more complex geometries, such as convergent or curved profiles, have not been thoroughly investigated.

The present study addresses these gaps by proposing a novel modification to the collector profile, aiming to significantly enhance the overall efficiency of SCPPs. In this study, the innovative approach involves using an elliptical constrained octagonal collector with a divergent chimney to assess its impact on design models for improved performance. Furthermore, the introduction of curvature to the collector profile, leveraging the geometric properties of ellipses and circular arcs to optimize the design. The innovative aspect of our work lies in the practical application of these complex geometric profiles, replacing the difficult-to-manufacture perfect parabolic mirrors with more feasible circular arc profiles that approximate parabolic curvature. This approach not only simplifies the manufacturing process but also retains the desired efficiency improvements. The manuscript is structured as follows: First, review of existing literature and discussed practical relationships observed in previous studies. Second section explains the methodology adopted and the geometries of the models taken for the study are discussed. The mathematical and experimental studies are discussed in Sects. 3 and 4 respectively. The last section discusses the key results of the research with validation of the same with key literatures.

Methodology

This study includes a collector profile with a conic constraint, mainly an elliptical profile, to validate its impact on system performance. Varying the collector inlet height is achieved by adjusting the semi-minor axis, "b," while reducing the collector leg height. An octagonal shape simplifies construction, creating a pyramidal appearance. The collector is subdivided into eight triangular portions, each with a semi-elliptical profile inclined at 10° in the pyramidal roof. Semi-minor axis variations from 0.01 to 0.03 m result in three elliptical profiles applied to both full and half-sloped collector configurations, yielding six models: FSCPP-1(b = 0.01 m), FSCPP-2(b = 0.02 m), FSCPP-3 (b = 0.03 m), HSCPP-1 (b = 0.01 m), HSCPP-2 (b = 0.02 m), and HSCPP-3 (b = 0.03 m). FSCPP/HSCPP denotes Full/Half inclined Semi-Elliptical Solar Chimney power plant. Figure 1a to Figure d provides schematic representations in 2D and 3D, while Fig. 1e illustrates the introduced curvature in the collector section.

Table 2 represents the geometric parameters of each model. Six SCPP models were designed with a chimney height of 4 m, collector radius of 2.6 m, collector inclination of 10°, chimney divergence of 2°, and top and bottom radiuses of 0.18 m and 0.37 m, respectively, using CATIA V5. Dimensions in this study were selected through approximations based on literature references and vivid numerical calculations. Here, the collector is an octagonal section inclined at 10°. The collector diameter is a circular periphery diameter described by intersecting edges around the octagonal collector, equivalent to its diagonal length. Dimensions other than b and h will be constrained as constants for models. The objective of this study is to validate the flow parameters in an SCPP equipped with a full, half-inclined semi-elliptical collector under 0.01, 0.02, and 0.03 m semi-minor heights through computational and experimental methods.

Figure 2 represents the overview of the proposed SCPP model considered in this study. To clarify the differentiation between Full Inclined Semi Elliptical Solar Chimney Power Plants (FSCPP-1,2,3) and Half-Inclined Semi Elliptical Solar Chimney Power Plants (HSCPP-1,2,3), it is indeed related to the geometric shape configuration of the collector profile. For the FSCPP models, the collector profile features a fully inclined semi-elliptical shape across the entire pyramidal collector roof, angled uniformly at 10°. This configuration implies that the entire collector surface is inclined and utilizes a semi-elliptical profile with variations in the semi-minor axis "b" (0.01 m, 0.02 m, 0.03 m) to achieve different collector inlet heights. Conversely, the HSCPP models incorporate a half-inclined design, where only half of the pyramidal collector surface is inclined with the semi-elliptical profile. In these models, while maintaining the same semi-minor axis values "b" (0.01 m, 0.02 m, 0.03 m), the collector is structured such that only half of the collector roof is inclined, while the other half remains horizontal. This half-inclination design is intended to assess how partial inclination impacts airflow characteristics and power output within the same structural parameters as FSCPP models.Therefore, the distinction between FSCPP and HSCPP models lies in the degree of surface inclination across the collector roof, which is a structural and performance-oriented design choice rather than a simple shape factor.

This study follows the workflow outlined in Fig. 4. Initially, computational analysis using ANSYS-FLUENT will be conducted for the designed models. Subsequently, experimentation on the best-performing computational fluid dynamics (CFD) models will be carried out in real-world conditions. The results will be compared with computational data and validated against previous studies, specifically the Straight Tower Inclined Collector Solar Chimney Power Plant (SSCPP), to conclude.

To address uncertainties in the validation results, the algorithmic flow begins by verifying the computational results of the best-performing models through error estimation within a valid range. Refer to Fig. 4 for a detailed algorithmic representation of the study's methodology.

Mathematical Formulation

Airflow flow is assumed to be steady and axially symmetric among turbulent characteristics. Here, Eq. 1[11] represents the mass flow rate inside the interior of SCPP. Equations 2, 3, 4[38–40] represents Mass, momentum,

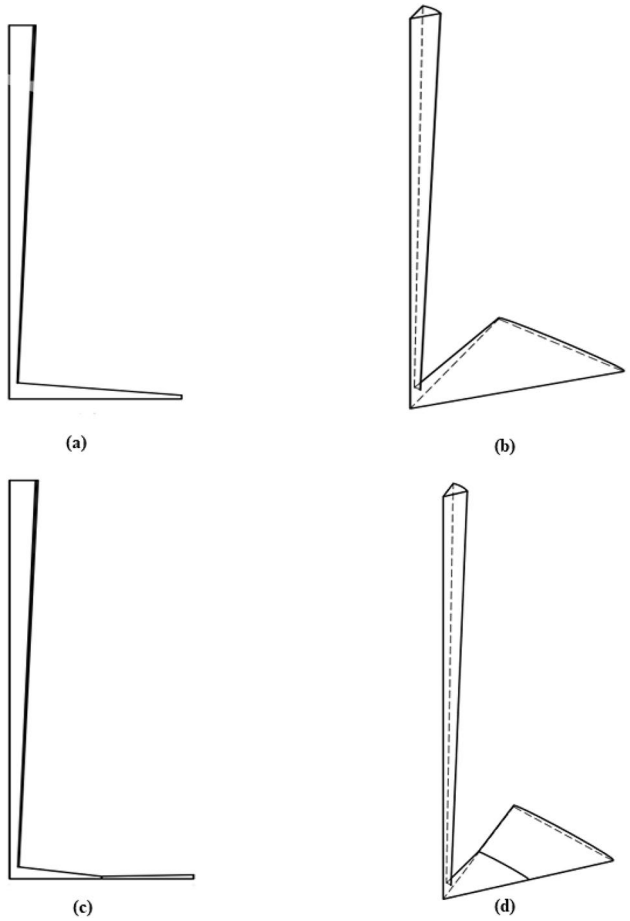


Fig. 1. (**a**) Elliptical Constrain in FSCPP, (**b**) Elliptical Constrain in HSCPP.

Models	Chimney Height (m)	Collector Diameter (m)	Collector Inlet Height		Chimney Inlet Diameter (m)	Chimney Outlet Diameter (m)	Inclination Angle of Collector (degree)
			Ellipse semi-minor axis, b (m)	Collector leg height, h (m)			
FSCPP 1	4	2.6	0.01	0.03	0.18	0.37	10
FSCPP 2	4	2.6	0.02	0.02	0.18	0.37	10
FSCPP 3	4	2.6	0.03	0.01	0.18	0.37	10
HSCPP 1	4	2.6	0.01	0.03	0.18	0.37	10
HSCPP 2	4	2.6	0.02	0.02	0.18	0.37	10
HSCPP 3	4	2.6	0.03	0.01	0.18	0.37	10

Table 2. Dimensional parameter of Six SCPP models.

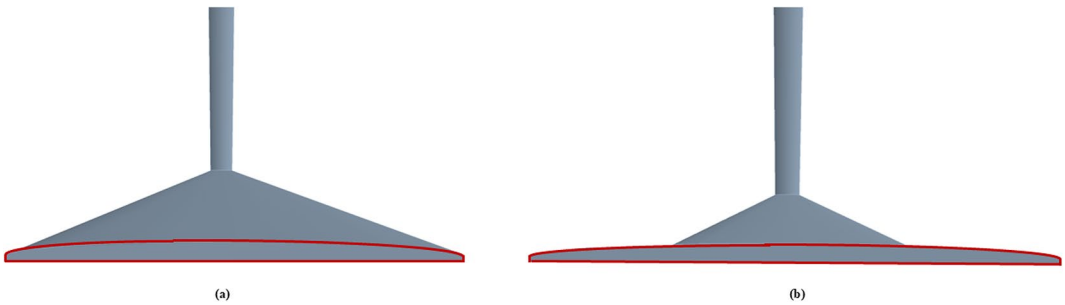


Fig. 2. (**a**) Elliptical Constrain in FSCPP, (**b**) Elliptical Constrain in HSCPP.

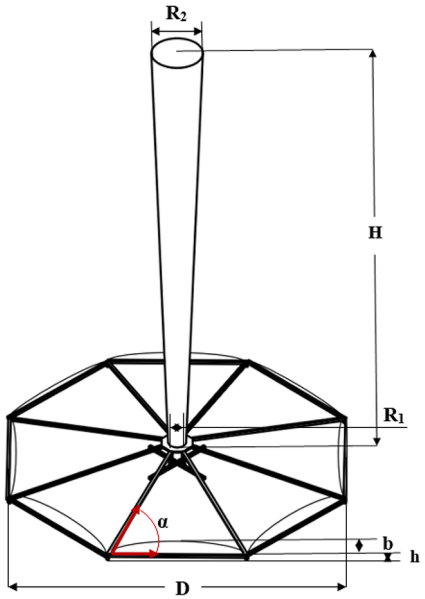


Fig. 3. Schematic Representation of SCPP.

energy and turbulent Eqs. (5–8)[41]were the basic governing principalities. For turbulence studies, a realizable k-ε model is preferred for a better approximation of turbulent kinetic energy (and turbulence dissipation rate) in the assumed flow regime. The discrete coordinate's model (9) under solar ray tracing is a radiation model assuming a real-scale solar environment on each model, which is crucial for approximate validation with an experimental case study. In Eq. (9), a, b, s, and n indicate absorptivity, intensity, scattered ring coefficient, and refractive index. Air density inside SCPP models was approximated through the Boussinesq expression mentioned in Eq. (10)[42]. The Rayleigh number for natural convection is used which is highly influenced by the () collector height, () thermal diffusion coefficient and ()kinematic viscosity. In the study carried out, the system is accepted as turbulent since the Ra number is higher than 10^9, which is the critical value[43]. The mathematical relations of these factors utilized in the computational study approach are specified below:

$$\dot{m} = \rho\, AV \tag{1}$$

$$\frac{\partial\ (\rho\, u)}{\partial\, t} + \nabla\ \cdot\ \rho\, \overrightarrow{V} = 0 \tag{2}$$

$$\rho\left[\frac{\partial\, \overrightarrow{v}}{\partial\, t} + \overrightarrow{V}\cdot\ \nabla\ \overrightarrow{V}\right] = -\nabla\, p + \mu\, \nabla^{\,2}\overrightarrow{V} + \frac{1}{3}\mu\, \nabla\ \left(\nabla\ \cdot\ \overrightarrow{V}\right) + \overrightarrow{F_b} \tag{3}$$

$$\frac{\partial\ (\rho\, e_t)}{\partial\, t} + \nabla\ \cdot\ \left[\overrightarrow{V}\,(\rho\, e_t + p)\right] = \nabla\ \cdot\ \left[k\nabla\, T + \left(\bar{\tau}\cdot\ \overrightarrow{V}\right)\right] + \dot{S}_g \tag{4}$$

$$\frac{\partial}{\partial\, t}\,(\rho\, k) + \frac{\partial}{\partial\, x_j}\,(\rho\, ku_j) = \frac{\partial}{\partial\, x_j}\left[\left(\mu\ + \frac{u_t}{\sigma\ _k}\right)\frac{\partial\, k}{\partial\, x_j}\right] + G_k + G_b - \rho\epsilon - Y_M + S_k \tag{5}$$

$$\frac{\partial}{\partial\, t}\,(\rho\epsilon) + \frac{\partial}{\partial\, x_j}\,(\rho\epsilon u_j) = \frac{\partial}{\partial\, x_j}\left[\left(\mu\ + \frac{\mu\ _t}{\sigma\ _\epsilon}\right)\frac{\partial\epsilon}{\partial\, x_j}\right] + \rho\, C_1 S\epsilon - \rho\, C_2\frac{\epsilon^2}{k + \sqrt{v\epsilon}} + C_{1\epsilon}\frac{\epsilon}{k}C_{3\epsilon}G_b + S_\epsilon \tag{6}$$

where

$$C_1 = max\left[0.43, \frac{\eta}{\eta\ + 5}\right];\ \eta\ = S\frac{k}{\epsilon}$$

$$\nabla\ \cdot\ (I_\lambda\ (\overrightarrow{r}, s)\ \overrightarrow{s}) + (a_\lambda\ + a_\epsilon)\, I_\lambda\ (\overrightarrow{r}, \overrightarrow{s}) = \ a_\lambda\, n^2 I_{b\lambda}\ + \ \frac{\sigma\ _s}{4\pi}\int_{\ 0}^{\ 4\pi} I_\lambda\,(\overrightarrow{r}, \overrightarrow{s})\varnothing\,(\overrightarrow{S}\ \cdot\ \overrightarrow{S'})d\Omega\,' \tag{7}$$

$$(\rho\ -\rho\ _0)\, g = -\rho\ _0\beta\ (T - T_0)\, g \tag{8}$$

Grid independence study

The grid independence study is crucial for accurate computational fluid dynamics (CFD) results, balancing the trade-off between simulation accuracy and computational speed. Using the Manzanares model, the study assesses fine, coarse, and medium mesh types, evaluating the number of elements and nodes. The average velocity

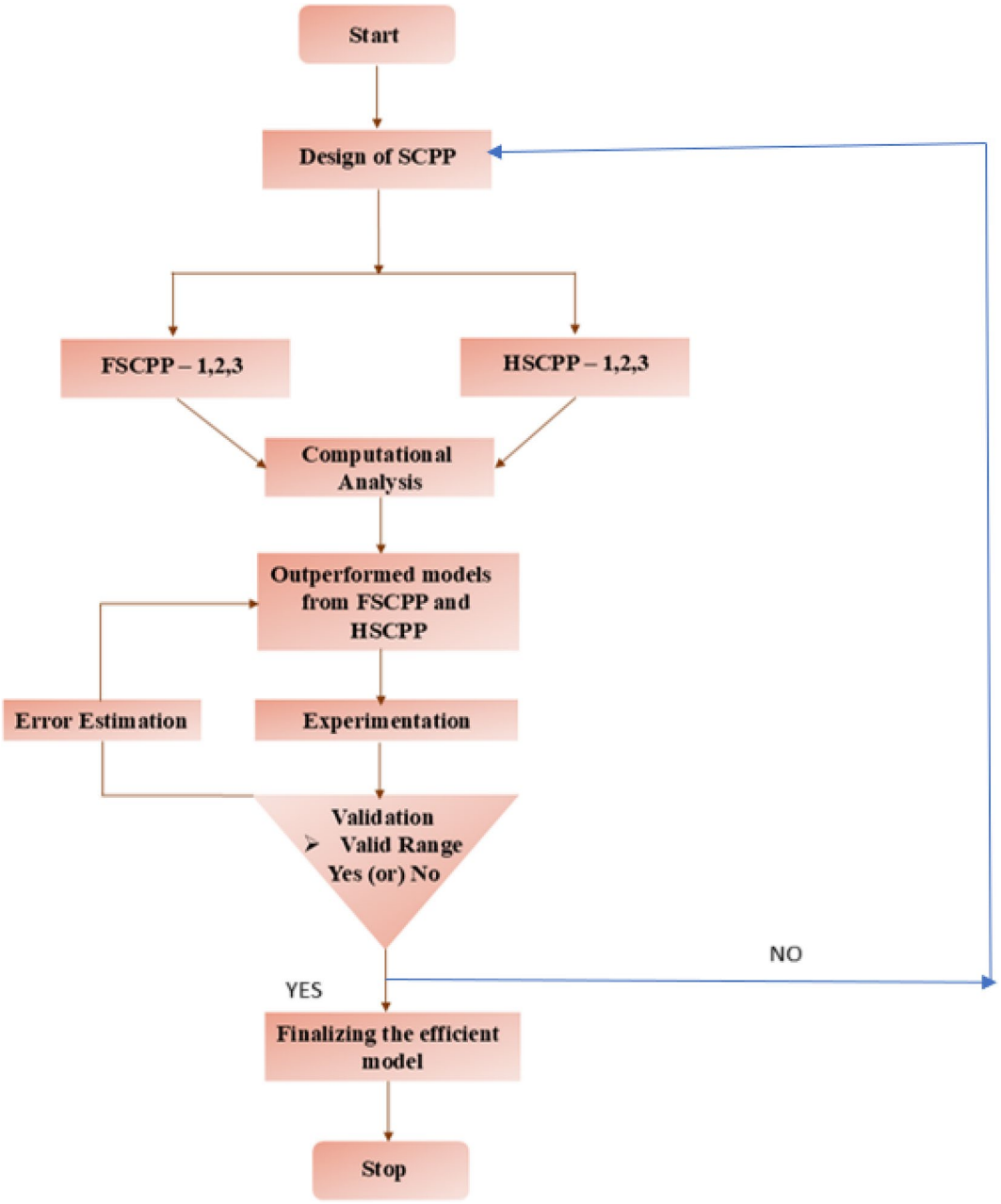


Fig. 4. Flow Chart representation of methodology.

magnitude serves as a reference parameter. The results guide the determination of a suitable number of elements for each model, ensuring accuracy without compromising computational efficiency. The study focuses on one-fourth of the Manzanares plant geometry for computational simulations, assuming symmetry on model sides.

The computational simulations carried out for each model in this study were considered under the one-fourth model, assuming the sides of each model have symmetry. This grid independence study considered several elements of the mesh zone to carry out simulation on Manzanares' model. Initially, the pilot plant geometry was simulated under these mesh conditions. The mesh conditions are established based on the grid independence study, with Fig. 5 (a) presenting the geometric view and Fig. 5 (b) depicting the mesh view. Initial simulations under these conditions reveal velocity variations, as shown in the velocity contour in Fig. 4(c). The satisfactory grid investigation results led to a shorter iteration period, providing mesh parameters for all six models in Table 3. The computational studies for each model adhere to the defined mesh parameters.

Key flow parameters, such as velocity and temperature rise, are detailed in Table 4. Comparisons with studies[44]and actual Manzanares pilot plant[4] results demonstrate minimal deviations within an acceptable range. Velocity variation across the geometry was represented by the velocity contour in Fig. 5c. Flow parameters achieved across the geometry were studied, and the maximum flow parameter (velocity, rise in temperature) was mentioned in the Table 4. The number of nodes for each of the six Semi-Elliptical Solar Chimney Power Plant

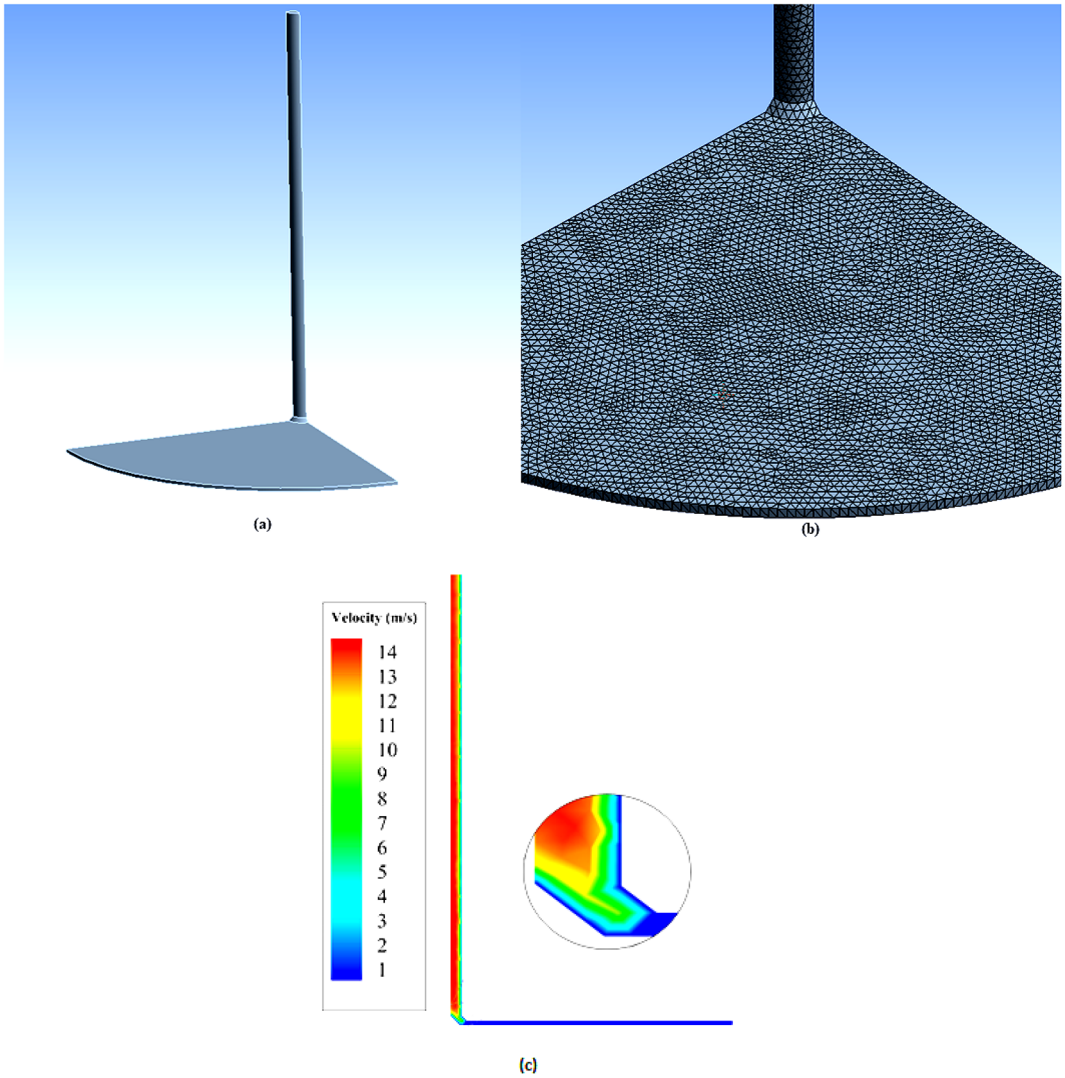


Fig. 5. Manzanares plant (**a**) 1/4th geometry view, (**b**) Mesh view (**c**) Manzanares Plant Velocity Contour.

Mesh type	Number of nodes	Number of cell counts	Maximum velocity (m/s)
Coarse	8994	275,000	13.14
Medium	10,951	325,000	13.1
Fine	13,199	480,000	13.14

Table 3. Details of Grid Independence Study.

Type	Velocity (m/sec)	Rise in temperature (K)
Manzanares[4]	15	20
[28]	14.81	20.96
Present work	14.9	18

Table 4. Validation of present study and results from Manzanares[4] and Sangi et al.[44].

Named sections	Zone type	Thermal conditions	Boundary conditions
Chimney	Wall	Heat Flux	Opaque, q = 0 W/m^2
Collector	Wall	Convection	Semi-transparent, q = 10 W/m^2
Ground	Wall	Heat Flux	Opaque, q = 0 W/m^2
Collector Inlet	Pressure Inlet	-	P = 0 pa
Chimney Outlet	Pressure Outlet	-	P = 0 pa

Table 5. Boundary Conditions.

Materials	Density (kg/m)	Specific Heat (J/kg K)	Thermal conductivity (W/m K)	Absorption Coefficient (m^{-1})	Refractive Index
Air	1.614 (Boussinesq)	1007	0.0263	0.00331	1
Galvanized Iron	7850	470	52	0.064	1
Poly carbonate sheet	1200	1170	0.19	0.01	1.585
Sand	2400	840	1.4	0.6	1

Table 6. Material values used in the study.

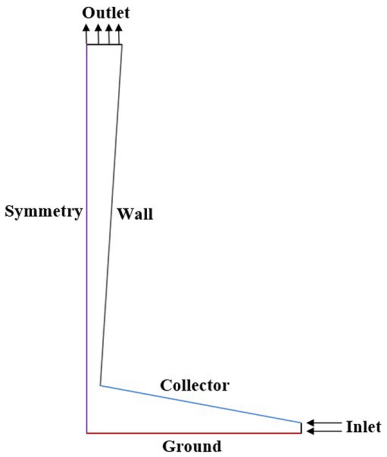


Fig. 6. Schematic Representation of Boundary Conditions.

(SCPP) mesh models is 77,528, 76,821, and 76,383 for FSCPP 1, FSCPP 2, and FSCPP 3, respectively. Whereas the element numbers are 393,018, 393,018, and 388,992 respectively. In the case of HSCPP 1, HSCPP 2, and HSCPP 3, the node counts are 79,409, 75,710, and 79,922, respectively, with corresponding element numbers of 392,095, 371,016, and 390,535. These mesh parameters were defined based on geometric proportions and guided the computational studies for each model.

Computational analysis

Computational Fluid Dynamics (CFD)-based analysis on each model was carried out under Ansys-Fluent. The gravitational effect is considered along the negative z direction as 9.81 m/s^2. Energy equations are enabled along with radiation model-discrete coordinates under the solar ray tracing technique[45]. The solar calculator was defined with the coordinates of Chennai-India was applied for solar irradiation; and the k-epsilon model under RNG specialization is defined for the turbulence effect. Here, air density is considered under the Boussinesq approximation[46,47]. Galvanized iron, polycarbonate, and sand specified under operating conditions of 1 atm pressure and 303 K temperature were chimney, collector, and ground materials.

Chimney, ground, is categorized under the wall zone heat flux condition at the boundary value, q = 0 W/m^2 as an opaque medium. The collector is modeled as a semi-transparent convective wall specified at q = 10 W/m^2. Collector inlet, chimney top zones defined as pressure inlet, outlet with boundary condition P = 0 pa[48]. The boundary conditions of each zone are represented in Table 5 and material values used in the study is shown in Table 6. The pictorial representation of the model defined by the boundaries is mentioned in Fig. 6.

As a solution method, the SIMPLE algorithm is executed for the relationship between air, velocity and pressure. Pressure interpolation is solved with the PRESTO technique. To model solar radiation, the solar ray tracing algorithm DO (discrete coordinates) is included in the simulation. For discretization, quadratic UPWIND is preferred[49]. For the density of the system air, the Boussinesq approach is applied to the model. Calculations initiated under hybrid initialization for defined mesh elements achieved a convergence of $10^{-6}$with smooth flow in solution iterations[50]. This setup was applied separately for each model, iterating solutions until convergence. Velocity, temperature, and pressure variations across the entire geometry were compared, revealing minimal differences in flow characteristics with variations in the collector section geometry. Temperature differences under ambient conditions were estimated from temperature profiles, showing positive values indicating higher temperature regions inside each system.

The temperature rise peaked at the chimney bottom for all models, resulting in a peak velocity regime at this position. FSCPP-1, FSCPP-2, FSCPP-3, HSCPP-1, HSCPP-2, and HSCPP-3 achieved maximum velocity magnitudes of 4.31, 4.23, 4.10, 4.49, 4.42, and 4.35 m/s, respectively, under maximum temperatures of 338 K, 336 K, 333 K, 339 K, 338 K, and 336 K. With an ambient temperature of 303 K, the maximum temperature differences were 35 K, 33 K, 30 K, 36 K, 35 K, and 33 K, respectively. The data indicates that FSCPP-1 exhibits greater maximum flow characteristics within the FCSPP group, while HSCPP-1 does the same in its group. Further details on these model behaviors will be discussed in the subsequent section. Both FSCPP-1 and HSCPP-1 were fabricated with the same materials used in simulation for experimentation under real environmental conditions.

Experimental investigation

From six models, two models with better effectiveness were separated to perform experiments. Initially, model fabrication progressed under constructing a 4 m chimney of 2° divergence, utilizing a galvanized iron sheet of thickness 0.002 m. For the collector, an octagonal frame is fabricated through metal bars by welding its edges. Polycarbonate sheets 0.002 m thick were installed on the collector frame, extending to the chimney bottom, forming a 10° inclined collector roof. Both sections, separately fabricated, were combined at the chimney bottom, elevating the entire body from the ground to 0.04 m through collector legs supported at each edge of the collector. Six holes at 0.2, 2, and 3.5 m, each parallel to the hole on the opposite side, along the chimney height, were drilled for velocity and temperature measurements. The schematic diagram (Fig. 7) represents the construction of experimental setup include in this study.

Thermocouples were installed at the prescribed locations on both chimney and collector Sects. 1,2, 3 are the locations across a chimney height of 3.5 m, 2.0 m, 0.2 m. Similarly, a, b, c are the locations for anemometer inlets provided to insert the anemometer head for velocity measurement. In the collector Sects. 4, 5, and 6 were the locations installed with thermocouples and d, e, f were the same locations to measure the velocity. These thermocouples were installed at centre, 1.2 m and 2.0 m in radial direction. Anemometer head was inserted into these locations parallel to the thermocouples to measure the velocities at the same locations. Numerous velocity and temperature data points can be obtained from the computational approach, but due to measuring apparatus restriction, only 9 data points were considered. These experimental data points were validated with the same data points from the computational data, where the position of these data points is same in both cases. The fabricated setup is shown in Fig. 8. Velocity in these positions is measured using a hot wire anemometer. K-type thermocouples connected to Arduino UNO R3 through the Max 6675 module were utilized for temperature measurement.

Entirely, six thermocouples were utilized for this study, with three installed at single-side chimney holes and the other three at the inlet (1.3 m), middle (0.65 m), and center (0 m) in the collector section. Each model was tested approximately for one day; from 9:00 a.m. to 4:00 p.m. Velocity and temperature measurements were

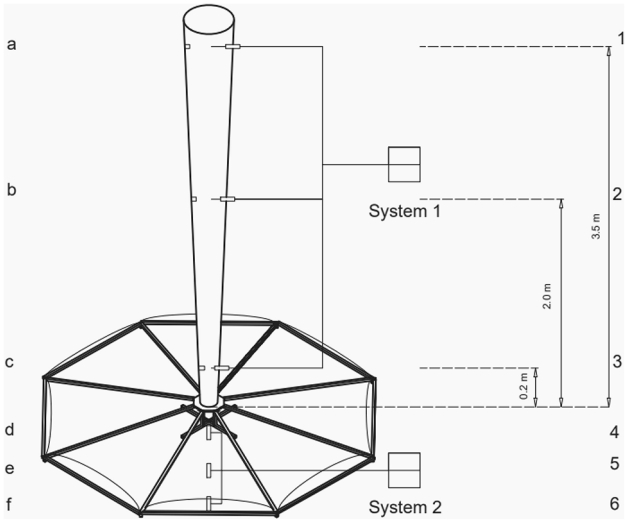


Fig. 7. Schematic Representation of Experimental Setup.



Fig. 8. Real time Experimental Setup considered in the study.

recorded at intervals of 30 min in the described period. Maximum flow characteristics of models identified at 1:30 p.m. The experimentation of a single model was repeated for the next two days, considering three active days of analysis for each model. FSCPP-1 and HSCPP-1 achieved maximum flow characteristics nearer to the chimney base, equivalent to computational magnitudes under an error approximation of less than 3%. The Hot Wire Anemometer Measures Temperature of accuracy range from ±2% to ±0.1%, also which measures velocity from 0.0 to 30.0 m/s with a resolution of 0.001.

Results and discussion

Comparisons and analysis of results from both approaches were conducted, focusing on maximum velocity and temperature rise, primarily situated slightly above the chimney base. These characteristics were observed in an extensive region within the collector and chimney interiors, with the maximum velocity concentrated in the chimney section from the base to a height of 0.2 m, referred to as the transition region. The temperature rise occurred in the chimney section, and the collector temperature profile indicated the maximum temperature region, extending from the ground area beneath the chimney base to the transition height. This ground area is termed the transition projected area. Velocity and temperature profiles for each model, visualized in Fig. 9 (a) to (l), depict variations in flow characteristics across SCPP interiors. Despite the different collector profiles, minimal differences were observed in the maximum parameters for each model. In the FSCPP subgroup with a complete collector inclination of 10° under a semi-elliptical profile, FSCPP-1 exhibited the highest maximum velocity at 4.31 m/s, with a temperature rise of 35 K.

In the HSCPP subgroup with a half-inclined collector profile, HSCPP-1 recorded the highest maximum velocity at 4.49 m/s, with a temperature rise of 36 K. Among these subgroups, FSCPP-1 and HSCPP-1 exhibited higher maximum flow parameter magnitudes. Velocity fluctuations across the entire system interior of the models were visualized in Fig. 9 (a), (c), (e), (g), (i), and (k). Minimal velocity at the collector inlet section led to a gradual increase until the transition region. Velocity rose from 0.431 m/s to 4.31 m/s in FSCPP-1 and from 0.3201 m/s to 4.49 m/s in HSCPP-1 in the transition regions. The chimney's inlet diameter of 0.18 m, due to divergence, increased to 0.1892 m at 0.2 m height, resulting in a minimal difference in diameter. This increase had a minimal effect on the cross-sectional area, maintaining constant velocity up to this height. Beyond this height, the deviation in the chimney cross-sectional area led to a gradual reduction in velocity. The continuity equation explains that an increase in cross-sectional area results in a reduction in velocity. The deviation of chimney walls increased along the chimney height, causing a reduction in flow velocity with a minimum velocity at the chimney top. Velocity reduction was initiated at 0.2 m and progressed until 2 m, which was gradual. From there, this reduction increased, reaching 0.86 m/s in FSCPP-1 and 0.96 m/s in HSCPP-1, aimed up to the chimney top. A similar variation in these models' temperature profiles specified the dependence of velocity parameters on heat distribution among the ground regions. Maximum heat accumulation on the ground is concentrated in a refined area beneath the transition region, termed the projected area of transition or projected area.

Maximum velocities of 4.31 m/s and 4.49 m/s were achieved in FSCPP-1 and HSCPP-1, respectively, with temperature rise being a crucial factor in this enhancement. Both models, maintaining a 10° collector inclination, exhibited concentrated heat distribution on a projected area, deviating from the uniform ground distribution seen in conventional collectors. The uneven temperature distribution across the ground was influenced by solar radiation refracted by the collector roof, converging on the projected area and initiating temperature enhancement in that region. The maximum temperature recorded was superior in HSCPP-1, reaching 338 K and 339 K, attributed to its smaller projected area. In FSCPP, the complete inclination is distributed as solar radiation across a projected area equivalent to half the ground area. In contrast, the half-inclined collector portion of HSCPP-1 created an even smaller projected area, approximately half of FSCPP-1. The efficient refraction of

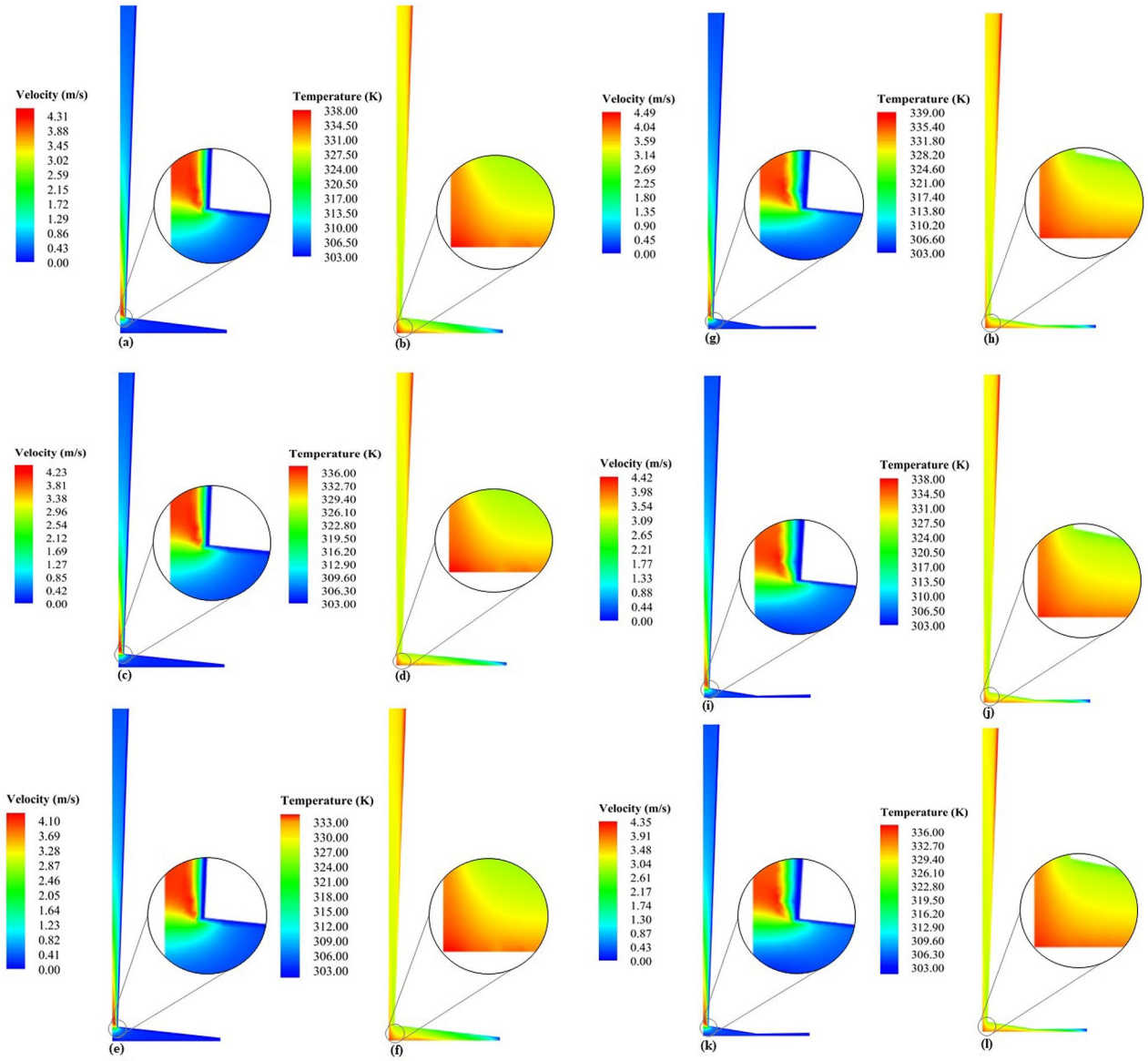


Fig. 9. (**a**) FSCPP-1 Velocity Contour, (**b**) FSCPP-1 Temperature Contour, (**c**) FSCPP-2 Velocity Contour, (**d**) FSCPP-2 Temperature Contour, (**e**) FSCPP-3 Velocity Contour, (**f**) FSCPP-3 Temperature Contour, (**g**) HSCPP-1 Velocity Contour, (**h**) HSCPP-1 Temperature Contour, (**i**) HSCPP-2 Velocity Contour, (**j**) HSCPP-2 Temperature Contour, (**k**) HSCPP-3 Velocity Contour, (**l**) HSCPP-3 Temperature Contour.

solar radiation in the half-inclined collector portion led to a convergence in its projected area, resulting in less heat distribution. The parallel collector portion in HSCPP-1 further contributed to this process, heating the remaining ground area, and resulting in a greater temperature magnitude. The temperature distribution in HSCPP-1 was concentrated on a smaller projected area, leading to a greater maximum temperature rise compared to FSCPP-1. The temperature distributions across the interior of all models were visualized in Fig. 9 (b), (d), (f), (h), (j), and (l). The airflow inside FSCPP-1 was visualized through the direction of streamlines in Fig. 8a. Streamlines, representing imaginary curves in the flow field, indicated the flow direction through their tangents. The maximum velocity was achieved up to a 0.2-meter chimney height, followed by a reduction in velocity until the chimney tops across the overall volume. Vortex regions were generated at half of the chimney height, with a higher-pressure gradient leading to a reverse flow. The interaction of the reverse flow with the incoming flow regime created mixed flow regions, resulting in a vortex structure with weakened intensity along the chimney height.

The ambient velocity within the collector gradually increased due to a 10° inclination, maintaining the maximum velocity in the transitional region. In the HSCPP-1 model, a maximum velocity of 4.49 m/s was achieved at 0.2 m, featuring half-collector inclination starting from a radius of 0.65 m. The air entered through the inlet into the collector, and due to the high temperature, the velocity increased up to the transition height with a divergence radius of 0.1892 m. The Straight Tower Inclined Collector Solar Chimney Power Plant (SSCPP) was

designed with a plane collector inclination of 10° and a cylindrical chimney with a divergence of 0° (see Fig. 10a-b). This model, created with similar dimensions to the previous models but neglecting the divergence angle, was used to compare velocity variations with FSCPP-1 and HSCPP-1 (see Fig. 10a). In contrast to the maximum velocities achieved in the previous models, the SSCPP model attained a maximum velocity of 2.52 m/s at the transitional region, nearly half the magnitude of the previous models. This decrease in velocity indicated the absence of chimney divergence for flow enhancement. The lack of divergence resulted in a longer transitional height, distributing the maximum velocity across the chimney length. The velocity reduction in this model was solely due to the frictional interaction of the flow with the chimney walls, resembling the flow in a circular pipe where velocity reduction occurs due to wall shear. The streamlined visualization of the flow regime across the model volume is illustrated in Fig. 10 (b).

Representation of variation of flow parameters (velocity and temperature) concerning the geometric parameters (chimney height and collector radius)

Variation of velocity and temperature concerning chimney height for all designed models

The velocity and temperature of all six models were plotted under chimney height in Fig. 11(a) and (b). The velocity curves (Fig. 11a) show minimal deviation among the models, as the increment in collector curvature height was only 0.01 m. The reduction in velocity along chimney height is influenced by the presence of a 2° divergence angle because of the expansion of air to the ambient. Temperature experiences a steeper reduction up to a length of 1.25 m (Fig. 11b) because of no slip boundary condition, followed by enhancement, and attributed to the use of galvanized iron as chimney material.

Variation of Velocity and Temperature with respect to Collector Radius for all designed models

Similarly, velocity (Fig. 11a) and temperature (Fig. 11b) variations in the collector were plotted against the collector radius to analyze their dependence on this parameter. The collector's velocity peaks near its center because of nozzle effect, which is also the center of the projected area on the ground. Air velocity near the boundary of the chimney was observed as a minimum when compared to the centre of the chimney because of no-slip boundary condition. The velocity gradually decreases away from the center. The maximum temperature is consistently reached at the central position for all models. The temperature profiles show a reduction from the center to the collector periphery, as depicted in Fig. 11(b), indicating the high-temperature region at central positions in each model.

Variation of temperature in different sections of chimney and collector with respect to time

The velocity variation over the collector area is shown in Fig. 12 (a), reveals that the velocity increment was very high in the center region, and collector temperature variations throughout the experimental period from 9:00 a.m. to 4:00 p.m. are depicted in Fig. 12(b). Temperatures were recorded every 30 min using K-type thermocouples at specific locations: chimney transition (0.2 m), chimney middle (2 m), chimney top (3.5 m), collector inlet (1.3 m), collector middle (0.65 m), and collector center (0 m). The entire duration was divided into 30-minute intervals, with each measurement taken within this timeframe. The maximum temperature was observed at 1:30 p.m. in the transition region. The transition region was further divided into two sections: the velocity enhancement region from the collector to the collector-chimney intersection (referred to as the collector transition) and from this intersection zone to a chimney height of 0.02 m (referred to as the chimney transition region).

Temperature exhibited an enhancement during the experimental period until 1:30 PM, followed by a reduction in both chimney and collector sections due to decreasing ambient temperatures due to continuous reduction in momentum of air. The temperature variations at different sections of the chimney and collector

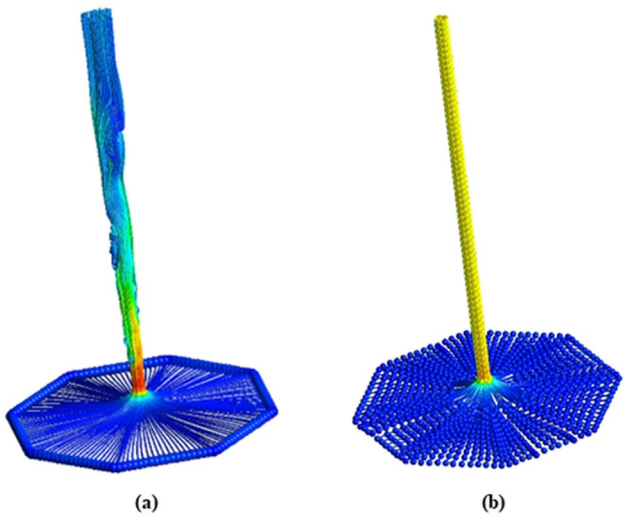


Fig. 10. Flow Visualization of Streamlines (**a**) FSCPP, (**b**) SSCPP.

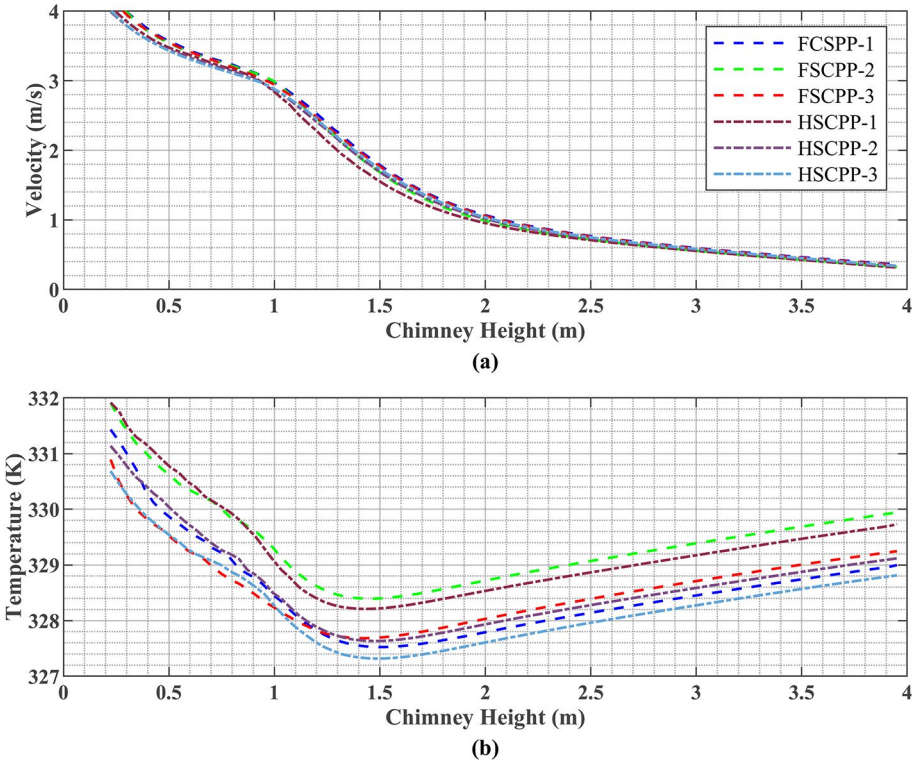


Fig. 11. (**a**) Variation of Velocity under Chimney Height for all models, (**b**) Variation of Temperature under Chimney Height for all models.

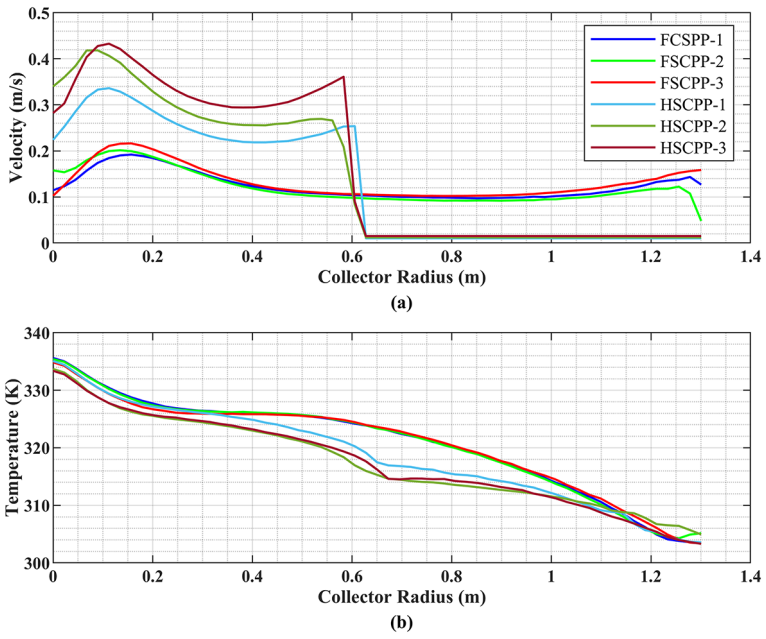


Fig. 12. (**a**) Variation of Velocity with Collector Radius for all models, (**b**) Variation of Temperature with Collector Radius for all models.

during this time were depicted in Fig. 13a. Each section experienced an increase in temperature until 1:00 p.m. – 1:30 p.m. Followed by a decline. Fluctuations in the plot profiles was due to the variation in solar radiation throughout the day during the experimental days. Note that the values are not indicated using any weighted average method. The maximum flow parameters attained from this experiment have an error approximation of up to 2% due to changes in ambient atmospheric conditions. The average magnitude of ambient temperature

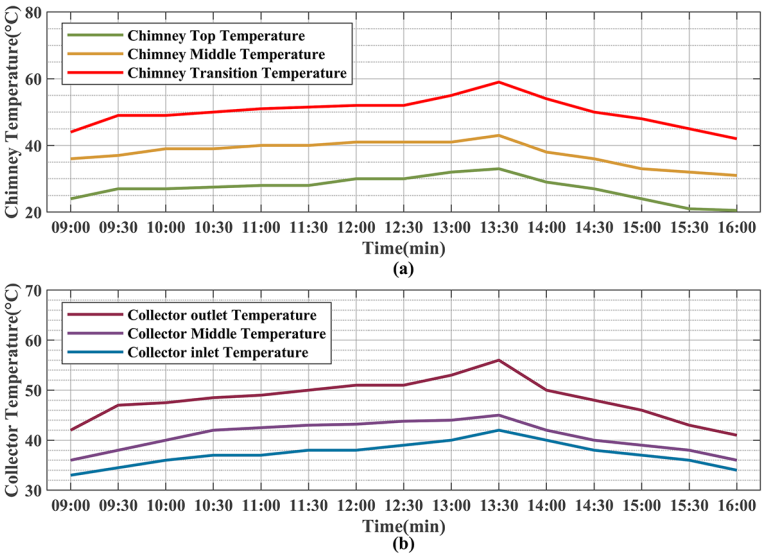


Fig. 13. (**a**) Variation of Temperature across different chimney sections, (**b**) Variation of Temperature across different collector sections.

fluctuation caused by weather condition alterations was 4 °C from the mean ambient temperature as shown in Fig. 13b.

Non-dimensional analysis on velocity, temperature profiles of FSCPP-1 and HSCPP-1

Non-dimensional analysis was conducted for the FSCPP-1 and HSCPP-1 models, where the positional velocity (V) across chimney height was normalized by the maximum velocity (Vmax), and the instantaneous temperature (T) at any point was normalized by the maximum temperature (Tmax). Both V/Vmax and T/Tmax were plotted against the divergent aspect ratio, i.e., Hchim/rd. In this ratio, the chimney height (Hchim) was non-dimensionalized with the divergent sectional radius across the chimney height (rd = 0.09 + 0.23x). Here, x represents the position across chimney height, and an increment in Hchim/rd values indicates a reduction in rd along x.

From the plots in Fig. 14 (a) and (b), it is observed that V/Vmax increases with the divergent aspect ratio up to 41.9, and then a reduction initiates from 41.9 to 42.8 because of the entrainment of air into the surroundings. This indicates that the velocity increment occurs in the range from rd = 0.093 m to 0.095 m. The maximum velocity ratio of 1 is attained at rd = 0.095, corresponding to the divergent section radius of the transitional height (0.2 m) where due to nozzle effect the velocity reaches the maximum value. In Fig. 14 (c) and (d), the temperature ratio of 1 is achieved at the normalized height of 42.8, equivalent to a rd of 0.093 m, where the height is 0.18 m, falling within the prescribed range of transitional height attributed to the fact that the heat transfer occur at faster rate as more air entrained inside the chimney. This non-dimensional approach supports the evaluation of both velocity and temperature variations under chimney height and radius in the same plot, providing a comprehensive understanding compared to the direct evaluation of these parameters.

Validation of the results with existing literatures412

The normalized collector velocity (u), expressed as a ratio to its maximum magnitude (u_{max}), and the collector radius ratio (r, the position measured from the collector center to an assumed position inside the collector periphery, with R_{coll}representing the collector radius) were plotted to analyze the variations in velocity and temperature within the collector region. These parametric variations in FSCPP-1, HSCPP-1, and SSCPP were compared with the findings of[4]and[15] for validation.

Variation of chimney velocity ratio with respect to positional ratio

The velocity ratio (V/Vmax) is plotted against the positional ratio (x/ri) for the FSCPP-1, HSCPP-1, and SSCPP models to compare velocity variation across chimney height in Fig. 15. The velocity ratio is defined as the ratio of the positional chimney velocity (V) to its maximum velocity (Vmax), while the position ratio (x/ri) represents the ratio of the position across chimney height (measured from the base as the chimney inlet), x, and the chimney inlet ratio, ri. FSCPP-1 and HSCPP-1 exhibit similar variations with minimal differences (see Fig. 15), achieving a maximum velocity ratio of 1 at position ratios of 0.09 and 0.07, respectively. This implies that the maximum velocities of 4.31 m/s and 4.49 m/s are attained at the transition height of 0.2 m. The SSCPP curve shows the maximum deviation from the remaining models due to the absence of chimney divergence. After a 0.5 H/R, the velocity ratio remains constant in SSCPP, while a 2° divergence in the remaining models leads to a further reduction in velocity magnitude across chimney height.

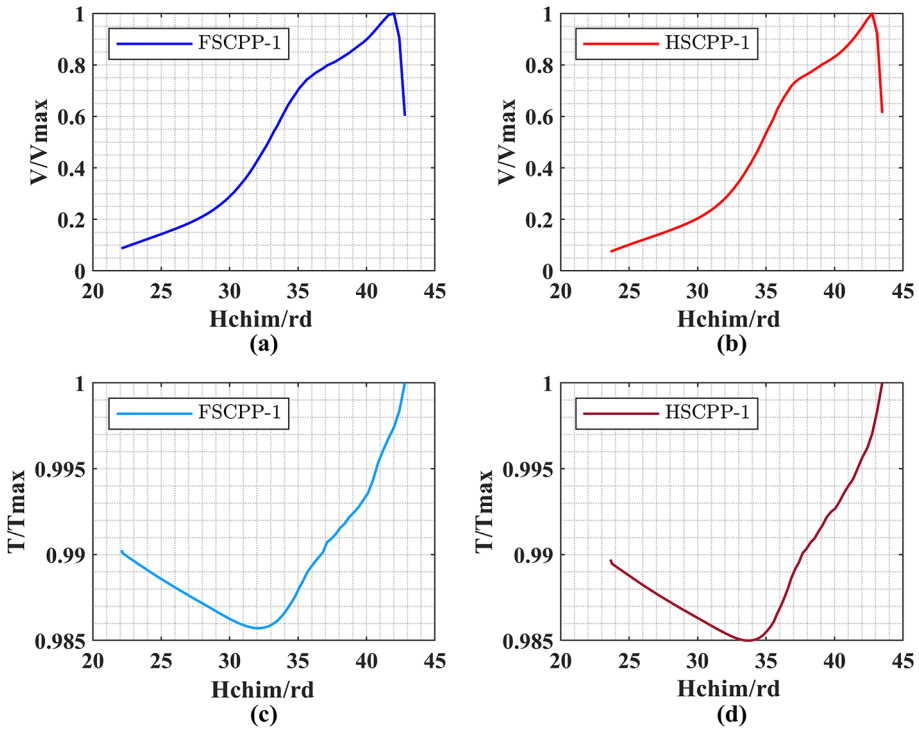


Fig. 14. Non-Dimensional Analysis on (**a**) Velocity ratio under divergent section aspect ratio for FSCPP-1, (**b**) Velocity ratio under divergent aspect ratio for HSCPP-1, (**c**) Temperature ratio under divergent aspect ratio for FSCPP-1, (**d**) Temperature ratio under divergent aspect ratio for HSCPP-1.

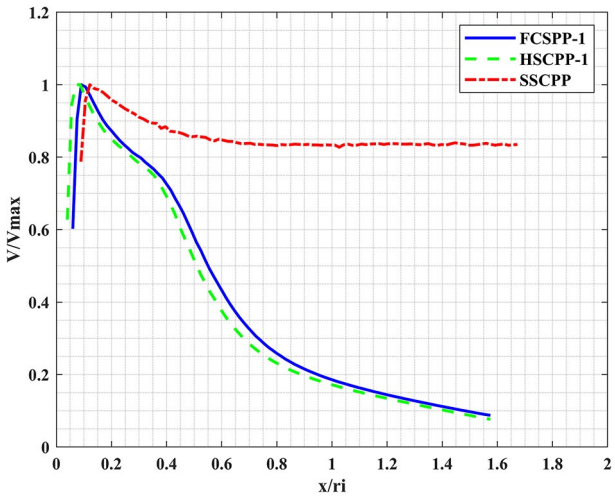


Fig. 15. Variation of Velocity Ratio under Positional ratio for FSCPP-1, HSCPP-1 and SSCPP.

Variation of collector velocity ratio with respect to collector radius ratio

The curve profiles (contained in Fig. 16) of the present models exhibit similarity in the variation of collector velocity ratio with respect to collector radius ratio. In HSCPP-1, the collector velocity undergoes small increments from a maximum radius ratio of 1 to 0.5, equivalent to a collector position radius of 0.65 (half collector radius). The velocity increment after this radius is attributed to the presence of a 10° collector inclination progressing from this position. A maximum velocity ratio of 1 is achieved at a radius ratio of 0, indicating the maximum velocity at the collector center. All curve profiles have an initial slope of 0° at V/Vmax of 1 and a final slope of 90° at maximum r/Rcoll. The change in slope between these two limits is different for the present study models compared to the literature studies[4,15]. For the present study models, the reduction in profile slopes is not gradual; instead, a sudden reduction occurs in the range of 0.85 to 0.9 (r/Rcoll). The difference is induced by the presence of an octagonal collector in the study models, where the flow from two triangular sections can be mixed at the

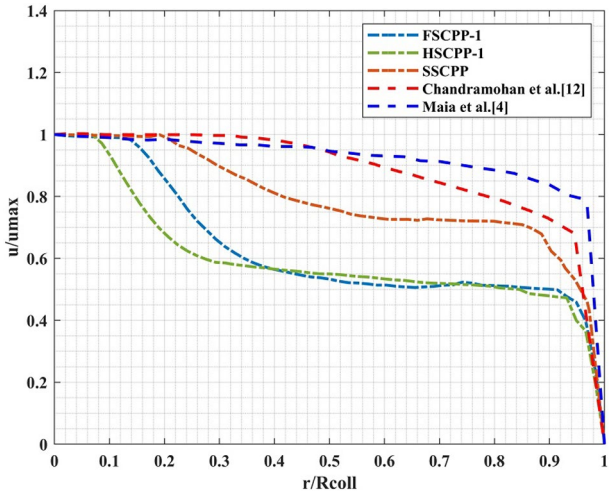


Fig. 16. Variation of Collector Velocity ratio under Collector Radius ratio FSCPP-1, HSCPP-1 and SSCPP.

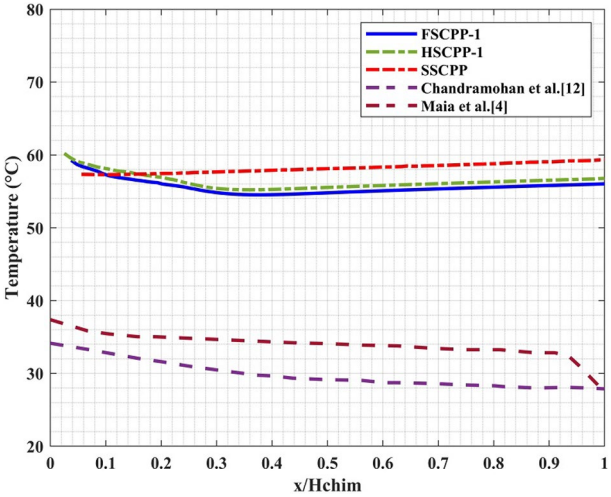


Fig. 17. Variation of Temperature under Chimney Height ratio for FSCPP-1, HSCPP-1 and SSCPP.

common inscribed sides of these sections. This results in a more significant reduction in flow velocity compared to a circular, inclined collector.

Variation of temperature with respect to chimney height ratio

The temperature in the chimney section is plotted with respect to the chimney height ratio, x/H_{chim}, where x is the positional height of the chimney and H_{chim} is the chimney height. FSCPP-1 and HSCPP-1 exhibit similar curve profiles, with minimal temperature differences of around 2 °C. In contrast, the SSCPP model, equipped with a straight chimney, maintains a linear temperature profile due to the absence of divergence. The present study models and the mentioned previous study models show a larger deviation of 20° in these temperature curve profiles, as depicted in Fig. 17. This deviation in the present study models is attributed to the use of galvanized iron as chimney material, which is a heat conductor.

In contrast, the existing studies employed polycarbonate and other non-metals as chimney materials. The present study models have a divergent chimney, resulting in an increased surface area across height. These two factors contribute to enhanced temperatures inside the chimney section. The maximum temperatures are achieved at x/H_{chim} ratios of 0.0375, 0.0425, and 0.05, equivalent to heights of 0.15, 0.17, and 0.2 m for the FSCPP-1, HSCPP-1, and SSCPP models, respectively. Temperature reduction initiates from these positions up to 3.26, 3.33, and 1.8 m. Beyond these locations, there is an enhancement in temperature due to the absorption of heat by the chimney wall.

The present study is thus carried out the study with elliptic collectors, this study is quite different from the other studies whose key parameters are mentioned in Table 7.

The present study introduces several distinct features compared to existing studies, as outlined in the comparative table. While many previous works employed straight chimney geometries and flat collector

Chimney geometry	Collector configuration	Collector material	Collector Diameter (m)	Chimney Height (m)	Chimney Diameter (m)	Vmax (m/s)	Temp. Rise (ΔT)	Ref
Divergent	Inclined	Polycarbonate transparent sheets		4	2.6	4.49	35	Present study
Straight	Flat	Glass	8.3	7.92	2.44	4	28	[14]
Straight	Flat	Glass	10	8	0.3	-	24.1	[39]
Straight	Inclined	Glass	10	8	0.3	-	24.1	[36]
Straight	Flat	Plastic	6.8	4	0.58	-	-	[52]
Straight	Inclined	Plastic	-	2.5	0.08	-	14	[28]
Straight	Flat	Glass	3	2	0.2	1.3	26.3	[30]
Straight	Flat	Plastic	2.75	3	0.32	1.32	13	[32]
Straight	Polycarbonate	Anti-refluxing glazed glass	3.5	6	0.6	5.5	11.4	[62]
Divergent	Flat	Glass	3	2	0.32	3	20–35	[65]
Straight	Inclined	Plastic	2	2	0.11	8	10	[66]
Straight	Flat	adhesive film of polyethylene	3.7	2.95	0.16	2.2	18	[67]
Straight	Inclined	-	3	6.3	0.32	2.25	3	[68]
Straight	Inclined	polyethylene	12	8	0.2	6	12.2	[69]
Straight	Inclined	Plastic	6	4	0.2	2.309	22	[70]

Table 7. Comparison of key parameters considered in literature and present study.

configurations with materials like glass and plastics, this study utilizes a divergent chimney geometry and a collector profile with a conic constraint, mainly an elliptical profile, to validate its impact on system performance. The divergent chimney increases the surface area along the height, which can enhance airflow dynamics and thermal performance.

The present research stands out by introducing an elliptical platform to the collector design, a novel approach that significantly improves system efficiency compared to previous studies. The elliptical profile enables variations in the collector curvature height (b = 0.01 m, 0.02 m, and 0.03 m), optimizing the flow dynamics and enhancing thermal performance. Unlike conventional flat collectors, the inclined collector design redistributes solar radiation away from the collector's periphery, leading to uneven ground heating and creating a high-temperature region beneath the transition area, termed the projected area. This effect contributes to increased velocity across the transition region, enhancing system performance.

In terms of performance, the present study achieves a maximum velocity (Vmax) of 4.49 m/s and a temperature rise (ΔT) of 35 K, which are competitive with or exceed the performance of other small-scale prototypes in the literature. For example, Ref. 38 reports a ΔT of 28 °C with a straight chimney and flat collector, while[15] reports a ΔT of 24.1 °C but lacks velocity data.

The innovative integration of a divergent chimney, semi-elliptical collector profiles, and adjustable inlet heights demonstrates the novelty of this study. These design modifications provide a pathway for performance enhancement and practical implementation, setting this work apart from prior studies focused on conventional straight chimneys and flat collectors. The comparative table emphasizes these differences and highlights the study's contributions to advancing SCPP design and performance.

Conclusion

The data obtained from both computational and experimental approaches were analyzed, yielding a satisfactory error approximation. The analysis involved examining plots of maximum velocity and temperature and studying the variation of these flow characteristics concerning collector radius and chimney height. The non-dimensional graphical approach for normalized parameters, including divergent aspect ratio, positional ratio, collector radius ratio, chimney velocity ratio, velocity ratio, and temperature, demonstrated alignment with the actual approach of dimensional parameters. In summary, the combination of a divergent chimney and convergent collector, induced by a semi-elliptical curved profile, led to enhanced velocity and temperature profiles at the transition region and projected area.

- The inclined collector transmitted solar radiation away from the collector periphery, resulting in uneven heating of the ground and a high-temperature region beneath the transition area, referred to as the projected area. This effect contributed to increased velocity across the transition region.
- Among the six models, the half-inclined semi-elliptical solar chimney power plant with a collector curvature height of 0.01 m achieved the maximum flow parameters. FSCPP-1 and HSCPP-1 exhibited maximum velocity and temperature rise magnitudes of 4.31 m/s, 35 K, and 4.48 m/s, 36 K, respectively.
- These models were experimented with external conditions from 9:00 a.m. to 4:00 p.m., with flow parameters measured at half-hour intervals, peaking at 1:30 p.m. The experimental results were similar to the maximum magnitudes achieved in the computational approach, with an error approximation of up to 5%.
- FSCPP-1 outperformed other models in its subgroup with velocity and temperature enhancements of up to 5% and 2%, respectively. HSCPP-1 outperformed its group models with a 41% enhancement.

- Validation with the SSCPP model revealed maximum velocity enhancements of up to 42% in the FSCPP and 44% in the HSCPP models.
- In these higher flow parameter magnitude models, HSCPP-1 outperformed FSCPP-1 with a 4% enhancement in maximum velocity magnitude and up to 2% in temperature magnitude. The minimal curvature heights included in this study (0.01 m, 0.02 m, and 0.03 m) resulted in minimal positive percentage enhancements.

Future studies could enhance numerical work by examining the impact of an elliptic air inlet gap on flow dynamics and performance parameters. The study also suggests the inclusion of a proper turbine design suitable for these lower velocity profiles, and future research should consider the impact of curvature constraints and turbine analysis on flow parameters, overall power output, and efficiency. The octagonal, semi-elliptical collector structure simplifies construction compared to traditional circular designs. For commercial deployment, this geometric simplification reduces material costs and time, making the design more feasible for large-scale implementation. The design can also be adapted for airflow-based cooling systems in industrial setups or used for water desalination processes in arid regions, showcasing its versatility beyond traditional SCPP applications.

Data availability

Data will be made available on reasonable request to the corresponding author.

Received: 29 August 2024; Accepted: 10 December 2024
Published online: 02 January 2025

References

1. Doppalapudi, A. T., Azad, A. K. & Khan, M. M. K. Advanced strategies to reduce harmful nitrogen-oxide emissions from biodiesel fueled engine. *Renew. Sustain. Energy Rev.* **174**, 113123 (2022).
2. Pablo-Romero, M. P., Sánchez-Braza, A. & Galyan, A. Renewable energy use for electricity generation in transition economies: Evolution, targets and promotion policies. *Renew. Sustain. Energy Rev.* **138**, 110481 (2020).
3. Cuce, P. M. et al. ANN and CFD driven research on main performance characteristics of solar chimney power plants: Impact of chimney and collector angle. *Case Stud. Therm. Eng.* **60**, 104568 (2024).
4. Maia, C. B., Ferreira, A. G., Valle, R. M. & Cortez, M. F. B. Theoretical evaluation of the influence of geometric parameters and materials on the behavior of the airflow in a solar chimney. *Comput. Fluids*. **38**, 625–636. https://doi.org/10.1016/j.compfluid.2008.06.005 (2009).
5. Hu, S., Leung, D. Y. C. & Chan, J. C. Y. Impact of the geometry of divergent chimneys on the power output of a solar chimney power plant. *Energy* **120**, 1–11. https://doi.org/10.1016/j.energy.2016.12.098 (2017).
6. Cuce, E. et al. Performance assessment of solar chimney power plants with the impacts of divergent and convergent chimney geometry, ˜the œInternational. *J. Low Carbon Technol.* **16**, 704–714. https://doi.org/10.1093/ijlct/ctaa097 (2021).
7. Von Backström, T. W. & Gannon, A. J. Solar chimney turbine characteristics. *Sol. Energy*. **76**, 235–241. https://doi.org/10.1016/j.solener.2003.08.009 (2004).
8. Cuce, E., Sen, H. & Cuce, P. M. Numerical performance modelling of solar chimney power plants: Influence of chimney height for a pilot plant in Manzanares, Spain. *Sustain. Energy Technol. Assess.* **39**, 100704. https://doi.org/10.1016/j.seta.2020.100704 (2020).
9. Toghraie, D., Karami, A., Afrand, M. & Karimipour, A. Effects of geometric parameters on the performance of solar chimney power plants. *Energy* **162**, 1052–1061. https://doi.org/10.1016/j.energy.2018.08.086 (2018).
10. Hassan, M., Ali, A. & Waqas Numerical investigation on performance of solar chimney power plant by varying collector slope and chimney diverging angle. *Energy* **142**, 411–425. https://doi.org/10.1016/j.energy.2017.10.047 (2018).
11. Cuce, E., Cuce, P. M. & Sen, H. A thorough performance assessment of solar chimney power plants: Case study for Manzanares. *Clean. Eng. Technol.* **1**, 100026. https://doi.org/10.1016/j.clet.2020.100026 (2020).
12. Amudam, Y. & Chandramohan, V. P. Influence of thermal energy storage system on flow and performance parameters of solar updraft tower power plant: A three dimensional numerical analysis. *J. Clean. Prod.* **207**, 136–152. https://doi.org/10.1016/j.jclepro.2018.09.248 (2019).
13. Yapıcı, E. Ö., Ayli, E. & Nsaif, O. Numerical investigation on the performance of a small scale solar chimney power plant for different geometrical parameters. *J. Clean. Prod.* **276**, 122908. https://doi.org/10.1016/j.jclepro.2020.122908 (2020).
14. Pasumarthi, N. & Sherif, S. A. Experimental and theoretical performance of a demonstration solar chimney model—Part II: experimental and theoretical results and economic analysis. *Int. J. Energy Res.* **22**, 443–461. https://doi.org/10.1002/(sici)1099-114x(199804)22:5 (1998).
15. Bernardes, M. A. D. S., Voß, A. & Weinrebe, G. Thermal and technical analyses of solar chimneys. *Sol. Energy*. **75**, 511–524. https://doi.org/10.1016/j.solener.2003.09.012 (2003).
16. Hu, S., Leung, D. Y. C. & Chan, J. C. Y. Numerical modelling and comparison of the performance of diffuser-type solar chimneys for power generation. *Appl. Energy*. **204**, 948–957. https://doi.org/10.1016/j.apenergy.2017.03.040 (2017).
17. Das, P. & Chandramohan, V. P. CFD analysis on flow and performance parameters estimation of solar updraft tower (SUT) plant varying its geometrical configurations, Energy Sources. Part a, Recovery, Utilization, and Environmental Effects **40,** 1532–1546. (2018). https://doi.org/10.1080/15567036.2018.1477881
18. Praveen, V., Das, P. & Chandramohan, V. P. A novel concept of introducing a fillet at the chimney base of solar updraft tower plant and thereby improving the performance: A numerical study. *Renew. Energy*. **179**, 37–46. https://doi.org/10.1016/j.renene.2021.07.038 (2021).
19. Zandian, A. & Ashjaee, M. The thermal efficiency improvement of a steam Rankine cycle by innovative design of a hybrid cooling tower and a solar chimney concept. *Renew. Energy*. **51**, 465–473 (2012).
20. Natarajan, R., Jayaraman, V., Dhanapal, B. & Sathyamurthy, R. Experimental and Computational Studies on Performance of a Solar Chimney Power Plant with Semiconvergent Collector and Divergent Chimney, (2020). https://doi.org/10.7546/crabs.2020.11.14
21. Natarajan, R., Jayaraman, V. & Sathyamurthy, R. Comparative studies on performance of solar towers with variable scale ratios. *Environ. Sci. Pollut. Res. Int.* **29**, 45601–45611. https://doi.org/10.1007/s11356-022-19079-0 (2022).
22. Murena, F., Gaggiano, I. & Mele, B. Fluid dynamic performances of a solar chimney plant: Analysis of experimental data and CFD modelling. *Energy* **249**, 123702. https://doi.org/10.1016/j.energy.2022.123702 (2022).
23. Koonsrisuk, A., Lorente, S. & Bejan, A. Constructal solar chimney configuration. *Int. J. Heat Mass Transf.* **53**, 327–333 (2009).
24. Li, J. Y., Guo, P. H. & Wang, Y. Effects of collector radius and chimney height on power output of a solar chimney power plant with turbines. *Renew. Energy*. **47**, 21–28 (2012).
25. Kasaeian, A. B., Molana, S., Rahmani, K. & Wen D. A review on solar chimney systems. *Renew. Sustain. Energy Rev.* **67**, 954–987 (2016).

26. Şen, H., Cüce, A. P. M. & Cüce, E. Impacts of collector radius and height on performance parameters of solar chimney power plants: a case study for Manzanares, Spain. *Recep Tayyip Erdoğan Üniversitesi Fen Ve Mühendislik Bilimleri Dergisi*. **2**, 83–104 (2021).
27. Cuce, P. M., Şen, H. & Cuce, E. Impact of tower diameter on power output in solar chimney power plants. *Gazi J. Eng. Sci.* **7**, 253–263 (2021).
28. Cottam, P. J., Duffour, P., Lindstrand, P. & Fromme, P. Effect of canopy profile on solar thermal chimney performance. *Sol. Energy*. **129**, 286–296 (2016).
29. Kasaeian, A. B., Heidari, E. & Vatan Sh. N. Experimental investigation of climatic effects on the efficiency of a solar chimney pilot power plant. *Renew. Sustain. Energy Rev.* **15**, 5202–5206 (2011).
30. Ghalamchi, M., Kasaeian, A. & Ghalamchi, M. Experimental study of geometrical and climate effects on the performance of a small solar chimney. *Renew. Sustain. Energy Rev.* **43**, 425–431 (2014).
31. Gholamalizadeh, E. & Kim, M. H. Multi-Objective Optimization of a Solar Chimney Power Plant with Inclined Collector Roof Using Genetic Algorithm. *Energies* **9**, 971 (2016).
32. Bouabidi, A., Ayadi, A., Nasraoui, H., Driss, Z. & Abid, M. S. Study of solar chimney in Tunisia: Effect of the chimney configurations on the local flow characteristics. *Energy Build.* **169**, 27–38 (2018).
33. Nasraoui, H., Driss, Z., Ayadi, A., Bouabidi, A. & Kchaou, H. Numerical and experimental study of the impact of conical chimney angle on the thermodynamic characteristics of a solar chimney power plant. *Proc. Institution Mech. Eng. Part. E J. Process. Mech. Eng.* **233**, 1185–1199 (2019).
34. Das, P. & Chandramohan, V. P. 3D numerical study on estimating flow and performance parameters of solar updraft tower (SUT) plant: Impact of divergent angle of chimney, ambient temperature, solar flux and turbine efficiency. *J. Clean. Prod.* **256**, 120353 (2020).
35. Tw, V. B. et al. State and recent advances in research and design of solar chimney power plant technology. IEEE PowerTech Conference 88, (2008).
36. Zhou, X., Yang, J., Xiao, B. & Hou, G. Experimental study of temperature field in a solar chimney power setup. *Appl. Therm. Eng.* **27**, 2044–2050 (2006).
37. Üçgül, İ. & Koyun, A. *Experimental investigations on performance and design parameters of solar chimney* (Directory of Open Access Journals, 2010).
38. El-Ghonemy Solar Chimney Power Plant without Collector. IOSR J. Electron. Commun. Eng. 11, 67–76. IOSR Journal of Electronics and Communication Engineering (IOSR-JECE) **11**, 67–76 (2016). (2016).
39. Al-Kayiem, H. H., Brebbia, C. A. & Zubir, S. S. *Energy and Sustainability v* (WIT, 2014).
40. Hu, S., Leung, D. Y. C. & Chen, M. Z. Q. Effect of divergent chimneys on the performance of a solar chimney power plant. *Energy Procedia*. **105**, 7–13 (2017).
41. Hassan, A., Ali, M. & Waqas, A. Numerical investigation on performance of solar chimney power plant by varying collector slope and chimney diverging angle. *Energy* **142**, 411–425 (2017).
42. Ahirwar, J. & Sharma, P. Analyzing the effect of solar chimney power plant by varying chimney height, collector slope and chimney diverging angle. *Int. J. Innovative Res. Technol.* **6**, 213–219 (2019).
43. Ming, T., De Richter, R. K., Meng, F., Pan, Y. & Liu, W. Chimney shape numerical study for solar chimney power generating systems. *Int. J. Energy Res.* **37**, 310–322 (2011).
44. Sangi, R., Amidpour, M. & Hosseinizadeh, B. Modeling and numerical simulation of solar chimney power plants. *Sol. Energy*. **85**, 829–838. https://doi.org/10.1016/j.solener.2011.01.011 (2011).
45. Ghorbani, B., Ghashami, M., Ashjaee, M. & Hosseinzadegan, H. Electricity production with low grade heat in thermal power plants by design improvement of a hybrid dry cooling tower and a solar chimney concept. *Energy. Conv. Manag.* **94**, 1–11 (2015).
46. Das, P. & VP, C. Performance characteristics of divergent chimney solar updraft tower plant. *Int. J. Energy Res.* **45**, 17159–17174 (2020).
47. Xu, Y. & Zhou, X. Performance of divergent-chimney solar power plants. *Sol. Energy*. **170**, 379–387 (2018).
48. Rincón-Mejía, E. *& De Las Heras, A. Sustainable Energy Technologies* (CRC, 2017).
49. Choi, Y. J., Kam, D. H., Park, Y. W. & Jeong, Y. H. Development of analytical model for solar chimney power plant with and without water storage system. *Energy* **112**, 200–207 (2016).
50. Yaswanthkumar, A. & Chandramohan, V. P. Numerical analysis of flow parameters on solar updraft tower (SUT) with and without thermal energy storage (TES) system. *J. Therm. Anal. Calorim.* **136**, 331–343 (2018).
51. Attig-Bahar, F., Sahraoui, M., Guellouz, M. S. & Kaddeche, S. Effect of the ground heat storage on solar chimney power plant performance in the South of Tunisia: Case of Tozeur. *Sol. Energy*. **193**, 545–555 (2019).
52. Salarpour, N. & Azadani, L. N. Optimization and evaluation of thermo-hydraulic performance of solar air heaters equipped with different roughness geometries. *Case Stud. Therm. Eng.* **61**, 105037 (2024).
53. Mahanand, Y. & Senapati, J. R. Thermo-Hydraulic Characteristics Evaluation of a triangular solar air heater duct having transverse ribs with gaps: an experimental study. *J. Sol. Energy Eng.* **146**, (2023).
54. Ridwan, H., Hafizh, M. R. & Fauzi Design and experimental test for solar chimney power plant: case study in Riau Province, Indonesia, IOP Conference Series. Materials Science and Engineering **403,** 012092 (2018). https://doi.org/10.1088/1757-899x/403/1/012092
55. Saad, M., Ahmed, N., Mahmood, M. & Sajid, M. B. Performance enhancement of solar updraft tower plant using parabolic chimney profile configurations: A numerical analysis. *Energy Rep.* **8**, 4661–4671. https://doi.org/10.1016/j.egyr.2022.03.134 (2022).
56. Nazari, S., Daghigh, R. & Part, B. Techno-enviro-exergo-economic and water hygiene assessment of non-cover box solar still employing parabolic dish concentrator and thermoelectric peltier effect, Process Safety and Environmental Protection/Transactions of the Institution of Chemical Engineers. Process Safety and Environmental Protection/Chemical Engineering Research and Design/Chemical *Eng. Res. Des.* **162** 566–582. https://doi.org/10.1016/j.psep.2022.04.006. (2022).
57. Raj, P. L. et al. Studies on divergent solar chimney subjected to variable collector configurartions. *Energy Sources Part. Recovery Utilization Environ. Eff.* **44**, 9522–9544. https://doi.org/10.1080/15567036.2022.2127981 (2022).
58. Al-Dabbas, M. A. The first pilot demonstration: solar updraft tower power plant in Jordan'. *Int. J. Sustain. Energ.* **31** (6), 399–410. https://doi.org/10.1080/1478646x.2011.589516 (2011b).
59. Zhou, X., Yang, J., Hou, G. & Bo Xiao and Experimental study of temperature field in a solar chimney power setup. *Appl. Therm. Eng.* **27**, 2044–2050 (2007).
60. Mekhail, T. et al. Experimental and theoretical performance of mini Solar Chimney Power Plant. *J. Clean. Energy Technol.* **5** (4), 294–298. https://doi.org/10.18178/jocet.2017.5.4.386 (2017).
61. Balijepalli, R., Chandramohan, V. P. & Kirankumar, K. Development of a small scale plant for a solar chimney power plant (SCPP): A detailed fabrication procedure, experiments and performance parameters evaluation. *Renew. Energy*. **148**, 247–260. https://doi.org/10.1016/j.renene.2019.12.001 (2019).
62. Motoyama, M. et al. Improving the power generation performance of a solar tower using thermal updraft wind. *Energy Power Eng.* **06** (11), 362–370. https://doi.org/10.4236/epe.2014.611031 (2014).
63. Nasraoui, H., Driss, Z., Ayedi, A. & Kchaou, H. Numerical and Experimental Study of the Aerothermal Characteristics in Solar Chimney Power Plant with Hyperbolic Chimney Shape. *Arab. J. Sci. Eng.* **44** (9), 7491–7504. https://doi.org/10.1007/s13369-019-03821-x (2019).

64. Al-Azawiey, S. S., Al-Kayiem, H. H. & Hassan, S. B. On the Influence of Collector Size on the Solar Chimneys Performance. In Proceedings of the MATEC Web of Conferences, Malacca, Malaysia, **25–27**, 131 (2017).
65. Ohya, Y., Wataka, M., Watanabe, K. & Uchida, T. Laboratory experiment and numerical analysis of a new type of solar tower efficiently generating a thermal updraft. *Energies* **9**, 1077 (2016).
66. Lal, S., Kaushik, S. C. & Hans, R. Experimental investigation and CFD simulation studies of a laboratory scale solar chimney for power generation. *Sustain. Energy Technol. Assess.* **13**, 13–22 (2016).
67. Ahmed, M. R. & Patel, S. K. Computational and experimental studies on solar chimney power plants for power generation in Pacific Island countries. *Energy Convers. Manag.* **149**, 61–78 (2017).
68. Ahmed, S. T. & Chaichan, M. T. A study of free convection in a solar chimney model. *Eng. Technol. J.* **29**, 2986–2997 (2011).
69. Golzardi, S., Mehdipour, R. & Baniamerian, Z. How collector entrance influences the solar chimney performance: Experimental assessment. *J. Therm. Anal. Calorim.* **146**, 813–826 (2021).

Acknowledgements

The authors extend their appreciation to the Deanship of Scientific Research at King Khalid University for funding this work under Grant No. RGP 2/306/44. The authors wish to express his sincere thanks to the honorable referees and the editor for their valuable comments and suggestions to improve the quality of the paper. Additionally, all authors would like to express their gratitude to the United Arab Emirates University, Al Ain, UAE, for providing financial support with UPAR Grant No. 12S122.

Author contributions

Rajamurugu Natarajan : Validation, Visualization, Writing – review & editing. S. Yaknesh: Writing – original draft, Validation, Methodology, Investigation, Formal analysis, Conceptualization. K B Prakash: Supervision, Writing – review & editing, Methodology, Investigation.Mohammed Al Awadh: Writing – original draft, Formal analysis, Conceptualization. Qasem M. Al-Mdallal: Visualization, Validation, Methodology, Investigation, Formal analysis, Conceptualization.

Declarations

Competing interests

The authors declare no competing interests.

Additional information

Correspondence and requests for materials should be addressed to Q.M.A.-M.

Reprints and permissions information is available at www.nature.com/reprints.

Publisher's note Springer Nature remains neutral with regard to jurisdictional claims in published maps and institutional affiliations.

Open Access This article is licensed under a Creative Commons Attribution-NonCommercial-NoDerivatives 4.0 International License, which permits any non-commercial use, sharing, distribution and reproduction in any medium or format, as long as you give appropriate credit to the original author(s) and the source, provide a link to the Creative Commons licence, and indicate if you modified the licensed material. You do not have permission under this licence to share adapted material derived from this article or parts of it. The images or other third party material in this article are included in the article's Creative Commons licence, unless indicated otherwise in a credit line to the material. If material is not included in the article's Creative Commons licence and your intended use is not permitted by statutory regulation or exceeds the permitted use, you will need to obtain permission directly from the copyright holder. To view a copy of this licence, visit http://creativecommons.org/licenses/by-nc-nd/4.0/.

© The Author(s) 2024